

# Exploring the stellar rotation of early-type stars in the LAMOST Medium-Resolution Survey. I. Catalog

WEIJIA SUN,<sup>1,2</sup> XIAO-WEI DUAN,<sup>1,2</sup> LICAI DENG,<sup>2,3,4</sup> RICHARD DE GRIJS,<sup>5,6</sup> BO ZHANG,<sup>7</sup> AND CHAO LIU<sup>2</sup>

<sup>1</sup>*Kavli Institute for Astronomy & Astrophysics and Department of Astronomy, Peking University, Yi He Yuan Lu 5, Hai Dian District, Beijing 100871, China*

<sup>2</sup>*Key Laboratory for Optical Astronomy, National Astronomical Observatories, Chinese Academy of Sciences, 20A Datun Road, Chaoyang District, Beijing 100012, China*

<sup>3</sup>*School of Astronomy and Space Science, University of the Chinese Academy of Sciences, Huairou 101408, China*

<sup>4</sup>*Department of Astronomy, China West Normal University, Nanchong 637002, China*

<sup>5</sup>*Department of Physics and Astronomy, Macquarie University, Balaclava Road, Sydney, NSW 2109, Australia*

<sup>6</sup>*Research Centre for Astronomy, Astrophysics and Astrophotonics, Macquarie University, Balaclava Road, Sydney, NSW 2109, Australia*

<sup>7</sup>*Department of Astronomy, Beijing Normal University, Beijing 100875, China*

## ABSTRACT

We derive stellar parameters and abundances (‘stellar labels’) of 40,034 late-B and A-type main-sequence stars extracted from the Large Sky Area Multi-Object Fiber Spectroscopic Telescope Medium Resolution Survey (LAMOST–MRS). The primary selection of our early-type sample was obtained from LAMOST Data Release 7 based on spectral line indices. We employed the Stellar LAbel Machine (SLAM) to derive their spectroscopic stellar parameters, drawing on Kurucz spectral synthesis models with  $6000\text{ K} < T_{\text{eff}} < 15,000\text{ K}$  and  $-1\text{ dex} < [\text{M}/\text{H}] < 1\text{ dex}$ . For a signal-to-noise ratio of  $\sim 60$ , the cross-validated scatter is  $\sim 75\text{ K}$ ,  $0.06\text{ dex}$ ,  $0.05\text{ dex}$ , and  $\sim 3.5\text{ km s}^{-1}$  for  $T_{\text{eff}}$ ,  $\log g$ ,  $[\text{M}/\text{H}]$ , and  $v \sin i$ , respectively. A comparison with objects with prior, known stellar labels shows great consistency for all stellar parameters, except for  $\log g$ . Although this is an intrinsic caveat that comes from the MRS’s narrow wavelength coverage, it only has a minor effect on estimates of the stellar rotation rates because of the decent spectral resolution and the profile-fitting method employed. The masses and ages of our early-type sample stars were inferred from non-rotating stellar evolution models. This paves the way for reviewing the properties of stellar rotation distributions as a function of stellar mass and age.

*Keywords:* Stellar rotation (1629), Astronomy data analysis (1858), Catalogs (205), Early-type stars (430), Stellar properties (1624)

## 1. INTRODUCTION

Early-type stars comprise hot, massive, and luminous stars of spectral types O, B, A, and early-F. They are short-lived and rare compared with late-type dwarfs, which are less massive. Most early-type stars are found in dense interstellar clouds in spiral arms or other dusty regions. As massive stars, they facilitate the chemical enrichment and reionization of the Universe, which makes them important contributors to the evolution of their host galaxies.

Early-type stars are very important for studies of Galactic and stellar structure. They are the progenitors of various types of supernovae (Poelarends et al. 2008) and can be sources of gamma-ray bursts (Langer 2012). During their lifetimes, they release much ultraviolet radiation, which rapidly ionizes the surrounding interstellar medium in giant molecular clouds, forming HII regions or Strömgren spheres. Massive early-type stars are useful probes of elemental abundances and tracers for mapping the spiral structure and disk of the Milky Way (Morgan et al. 1952; Venn 1995; Carraro et al. 2010, 2017; Xu et al. 2018).

Most early-type stars have significantly higher rotation rates than solar-type and low-mass stars (Glebocki et al. 2000), due to their higher initial angular momenta, shorter contraction timescales to the zero-age main sequence (ZAMS), lack of deep convective envelopes, and strong magnetic fields (except for chemically peculiar stars). For instance, Be stars are B-type main-sequence stars with Balmer-line emission (Rivinius et al. 2013). The latter is believed to originate from their decretion disks, fed by mass ejected from the central stars due to rapid rotation (up to  $\sim 350\text{ km s}^{-1}$ ). Binarity is another key parameter that is different between early-type stars and their late-type

counterparts. The overall multiplicity frequency of main-sequence stars is a steep, increasing, monotonic function of spectral type from late to early types (Duchêne & Kraus 2013).

Precise and accurate stellar parameters derived from stellar spectra are necessary to understand early-type stars. Thanks to rapid improvements in modern observing facilities, we can now access large numbers of spectra from large spectroscopic surveys, e.g. the Large Sky Area Multi-Object Fiber Spectroscopic Telescope survey (LAMOST; Deng et al. 2012), the Sloan Digital Sky Survey (SDSS; Eisenstein et al. 2011), the Apache Point Observatory Galactic Evolution Experiment (APOGEE; Majewski et al. 2017), or the *Gaia* Radial Velocity Spectrometer (Cropper et al. 2018), which provide unprecedented opportunities to unravel the stellar population properties of large stellar samples. Liu et al. (2019) presented 22,901 stellar spectra of OB stars identified in LAMOST Data Release (DR) 5 based on their distribution in the space defined by their spectral line indices. A similar approach was applied by Guo et al. (2021a). These authors reported 10,608 early-type stars from LAMOST DR7 and estimated the binary fractions of different spectral types.

To derive stellar ‘labels’ (stellar parameters and abundances), common practice is to match stellar spectra and model templates using Balmer and metal lines. In recent years, machine-learning algorithms have been introduced, which have proved efficient in processing large databases (Ting et al. 2019; Xiang et al. 2019). Zhang et al. (2020a) reported the implementation of a data-driven method based on support vector regression (SVR), known as the Stellar LAbel Machine (SLAM). It can produce stellar labels for a wide range of spectral types in LAMOST DR5 with high efficiency.

Here, we undertake a survey of early-type stars in LAMOST DR7, based on a sample size that is more than ten times larger than the previously largest database (Zorec & Royer 2012). We construct a data-driven model for medium-resolution spectra based on the SLAM model trained by ATLAS12 atmospheric models (Kurucz 2005). We compile a catalog composed of more than 40,000 stars with effective temperatures of  $7000 \text{ K} \leq T_{\text{eff}} \leq 14,500 \text{ K}$  and derive their stellar labels ( $T_{\text{eff}}$ ,  $\log g$ ,  $[M/H]$ , and  $v \sin i$ ) and fundamental parameters (masses and ages).

This article is organized as follows. In Section 2, we introduce the primary selection of our early-type candidates from the LAMOST data. Our application of the SLAM method to derive stellar labels, as well as the results of our validation, are presented in Section 3. The final catalog, including estimates of the fundamental stellar parameters and possible contamination, is described in Section 4. Finally, conclusions are drawn in Section 5.

## 2. DATA

### 2.1. Primary selection

LAMOST is a 4-meter quasi-meridian reflective Schmidt telescope equipped with 4000 fibers across its  $5^\circ$  field-of-view focal plane (Cui et al. 2012; Zhao et al. 2012). Following the initial low-spectral-resolution ( $R \sim 1800$ ) survey (LRS), conducted from 2011 to 2018 (LAMOST-I; Luo et al. 2015), LAMOST has been conducting a medium-resolution survey (MRS),  $R \sim 7500$ , with its upgraded spectrographs (LAMOST-II; Liu et al. 2020). The blue cameras of each spectrograph cover the wavelength range from 4950 Å to 5350 Å, while the red cameras cover 6300 Å to 6800 Å. With a single exposure time of 1200 s, the median signal-to-noise ratio (SNR) can reach values in excess of 5 for stars with *Gaia*  $G$ -band magnitudes  $G < 14.5$  mag. The SNR of co-added spectra composed of three 1200 s spectra can reach 10 at  $G = 14.5$  mag.

MRS DR7 contains 11,422,346 single-exposure and 2,968,667 co-added spectra (encompassing both the blue and red bands), which are tabulated in the LAMOST MRS General Catalog. The LAMOST data reduction pipeline subtracts the sky background and removes the Earth’s atmospheric telluric absorption in four bands, including the  $B$  band (Zhongrui 2013). The LAMOST team also released the LAMOST MRS Parameter Catalog, a subsample of 807,319 spectra whose stellar parameters and chemical abundances were estimated using various pipelines. The effective temperatures, surface gravities, and metallicities were determined by the LAMOST Stellar Parameter pipeline (LASP), whereas the rotational velocity was measured by matching with ELODIE templates. The elemental abundances were estimated using a deep-learning method (Wang et al. 2020).

To compile our primary catalog of early-type ( $T_{\text{eff}} > 7000 \text{ K}$ ) candidates, we selected the co-added spectra from the LAMOST MRS General Catalog and cross-matched them with *Gaia* early DR3 (EDR3; Gaia Collaboration et al. 2021). Compared with *Gaia* DR2 (Gaia Collaboration et al. 2018), EDR3 represents a significant improvement as regards estimates of the parallax systematics, both globally (Lindegren et al. 2021) and locally (Ren et al. 2021). Lindegren et al. (2021) published the parallax zero-point based on their analysis of quasars, binary stars, and the Large Magellanic Cloud. We adopted the photo-geometric distance estimates of Bailer-Jones et al. (2021)—who inferred distances from EDR3 parallaxes (corrected for the parallax zero-point) based on a three-dimensional Galactic model—as the distances

of our candidates. We also cross-matched our candidates with the Two Micron All Sky Survey (2MASS; [Skrutskie et al. 2006](#)) for extinction correction (see Section 4.1). As our preliminary selection criteria, we rejected those objects with effective temperatures below 6500 K (in practice below 7000 K to avoid removal of objects with incorrect temperature estimates) or SNRs less than 15.

Next, we selected those stars with accurate *Gaia* astrometric and photometric parameters following [Riello et al. \(2021\)](#). The renormalized unit weight error (RUWE), introduced after *Gaia* DR2 ([Arenou et al. 2018](#)), was adopted as a goodness-of-fit indicator (`ruwe` < 1.4). Objects with a close separation on the sky, less than 0.7'' ([Gaia Collaboration et al. 2021](#)), cannot yield reliable measurements. Therefore, they were rejected by imposing the criterion `duplicated_source==True`. We further used the corrected BP and RP flux excess factor  $C^*$ , introduced by [Riello et al. \(2021\)](#), to quantify the impact of variations in the local background level. The latter may affect the  $G_{BP}$  and  $G_{RP}$  integrated photometry. Equation 18 of [Riello et al. \(2021\)](#) was used to select a sample of well-behaved, isolated stellar sources with good-quality photometry. No saturation correction was applied, because the bright stars in our sample do not reach the brightness levels where saturation becomes an issue. As the final step, we rejected candidates with relative parallax errors larger than 10%.

## 2.2. Line indices

We further used the objects' spectral line indices to select early-type candidates. Line indices provide a mapping of the effective temperature without the caveats associated with extinction correction and flux calibration ([Liu et al. 2015](#)). A line index, in terms of its equivalent width (EW), is defined as ([Worthey et al. 1994](#))

$$\text{EW} = \int \left[ 1 - \frac{f_{\text{line}}(\lambda)}{f_{\text{cont}}(\lambda)} \right] d\lambda, \quad (1)$$

where  $f_{\text{line}}(\lambda)$  and  $f_{\text{cont}}(\lambda)$  are the fluxes of the spectral line and the continuum, respectively, and  $\lambda$  is the rest-frame wavelength.

Normalization of the spectra and transformation to the rest frame was done using the `laspec`<sup>1</sup> package ([Zhang et al. 2021](#)). In brief, we normalized our spectra by iteratively fitting a spectrum three times with a spline function and rejecting pixels deviating by more than  $3\sigma$  from the median values in 20 Å windows. Following normalization, the radial velocities,  $v_R$ , were estimated using the cross-correlation function method with respect to a collection of synthetic spectra based on the ATLAS9 model atmospheres ([Allende Prieto et al. 2018](#)). Because of the narrow wavelength coverage of both the blue and red spectrographs ( $\sim 400$  Å), continuum fluxes may be affected by the non-uniform spectral response function, especially toward the edges. Therefore, we calculated the relative flux ratios by normalization of the entire spectrum, instead of using the pseudo-continuum (e.g. [Liu et al. 2015](#); [Guo et al. 2021a](#)). Note that there might be some offset between the blue and red arms. Therefore, we applied the cross-correlation technique to both arms and transformed the red and blue spectra to the rest frame separately. We discarded those sources with  $|v_R| > 250 \text{ km s}^{-1}$  since they are probably affected by bad pixels suffering from strong cosmic rays or contaminated by emission lines arising either from their surrounding disks, or nearby HII regions.

In Figure 1, we present three sample spectra characterized by different effective temperatures from LAMOST MRS DR7. Observations of the same object obtained with the blue and red arms are shown in the left and right panels, respectively. The wavelength scale was transformed to the rest frame and fluxes were normalized to the pseudo-continuum, as described above. The best-fitting models determined by application of the SLAM method are shown as orange curves. The vertical red bands represent the wavelength ranges covering Mg I *b* and H $\alpha$ , which were used in our selection of the line indices. The top and bottom panels represent spectra of two stars with small projected rotational velocities ( $v \sin i < 100 \text{ km s}^{-1}$ ), while the middle panel shows a spectrum that is affected by strong rotational broadening.

Figure 2 shows the stellar loci in the parameter space defined by the line indices of H $\alpha$  (6548.0–6578.0 Å) and Mg I *b* (5160.12–5192.62 Å, reflecting integration over the three main Mg I features at 5167, 5172, and 5183 Å) for the selected MRS sample objects. The contours show the number densities in dense regions. Line indices from the ATLAS atmospheric models are overplotted for reference, color-coded by their effective temperature. The dense cluster at  $\text{EW}_{\text{H}\alpha} \sim 4 \text{ \AA}$  represents the low-temperature sample objects ( $T_{\text{eff}} < 6500 \text{ K}$ ) remaining following the initial temperature selection. There is an elongated aggregation at  $\text{EW}_{\text{H}\alpha} \sim 2 \text{ \AA}$ , which is mostly composed of late-type stars

<sup>1</sup> <https://github.com/hypergravity/laspec>

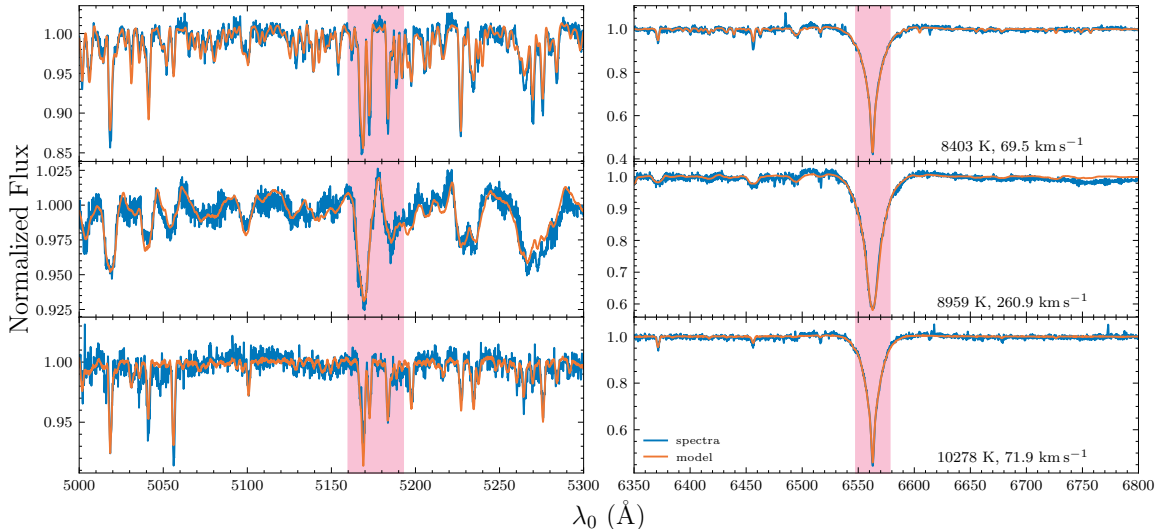


**Figure 1.** Normalized sample spectra, in the rest frame, from LAMOST MRS DR7 (blue) and the corresponding best-fitting models (orange) determined by the SLAM algorithm (see Section 3). Blue and red segments of the same object are shown in the left and right panels, respectively. The best-fitting effective temperatures,  $T_{\text{eff}}$ , and the projected rotational velocities,  $v \sin i$ , are listed in the bottom right corners. The red bands correspond to the spectral regions covering Mg I  $b$  (5160.12–5192.62 Å) and H $\alpha$  (6548.0–6578.0 Å).

with  $T_{\text{eff}} < 3100$  K that were missed in the LASP, while another aggregation is located at bottom right around 9400 K. The latter is an artifact caused by a concentration in the line indices parameter space (see Section 4.1).

To further avoid contamination by late-type stars, we rejected candidates with  $T_{\text{eff}} < 7000$  K (the shadowed area in Figure 2). Finally, we were left with 84,382 early-type candidates with decent SNRs (with median SNR values in excess of 40). As the next step in our data processing, stellar labels ( $T_{\text{eff}}$ ,  $\log g$ ,  $[M/H]$ , and  $v \sin i$ ) of each star in this reduced sample were extracted. We will outline the adopted method in the next section.

### 3. METHOD

SLAM is a data-driven method to estimate precise stellar labels from spectra based on SVR. Compared with other attempts, also based on SVR (e.g. Li et al. 2015), SLAM applies a generative model that automatically adjusts the model complexity and extracts information from the stellar spectra. SLAM’s performance on application to the LAMOST LRS (Zhang et al. 2020a) and MRS (Zhang et al. 2020b) spectra has been inspected, and the approach has been applied to various stellar populations (e.g. Guo et al. 2021b; Li et al. 2021).

#### 3.1. Training

Data-driven methods (e.g. Ness et al. 2015; Ting et al. 2017b) presume that the stellar labels of the training set are known accurately and precisely. Ideally, the training set is composed of observed spectra with high SNRs that have high-fidelity labels, either from a reference set built from well-studied objects that have been observed in the context of the survey (Hou et al. 2015) or from a common subset taken from a higher-resolution survey (Ting et al. 2017b). Unfortunately, such a training set containing a large collection of early-type stellar labels is not available. Therefore, we used a set of mock stellar spectra from ATLAS12 atmospheric models to build the training set.

However, our stellar labels are referenced to the set of model spectra adopted. For instance, the effective temperatures derived for chemically peculiar stars—which are prevalent especially among A-type stars (Preston 1974)—depend on which lines are used (Ca II K, Balmer H, metallic lines; Gray & Corbally 2009). Our sample probably also includes shell stars (e.g., Pleione; Gulliver 1977), which have narrow absorption lines associated with cooler plasma that originates in a gas disk projected against the stellar photospheres. In this paper, the results for such objects depend on which features are covered by the blue and red segments of the observed MRS spectra. Also note that the adopted ATLAS12 model is a local thermodynamic equilibrium (LTE) spectral model that does not take into account the presence of non-LTE (NLTE) effects. The atmospheres of cool stars are well described by LTE model atmospheres, but stars of spectral types earlier than A require a detailed treatment of NLTE effects because of the high energy densities of their

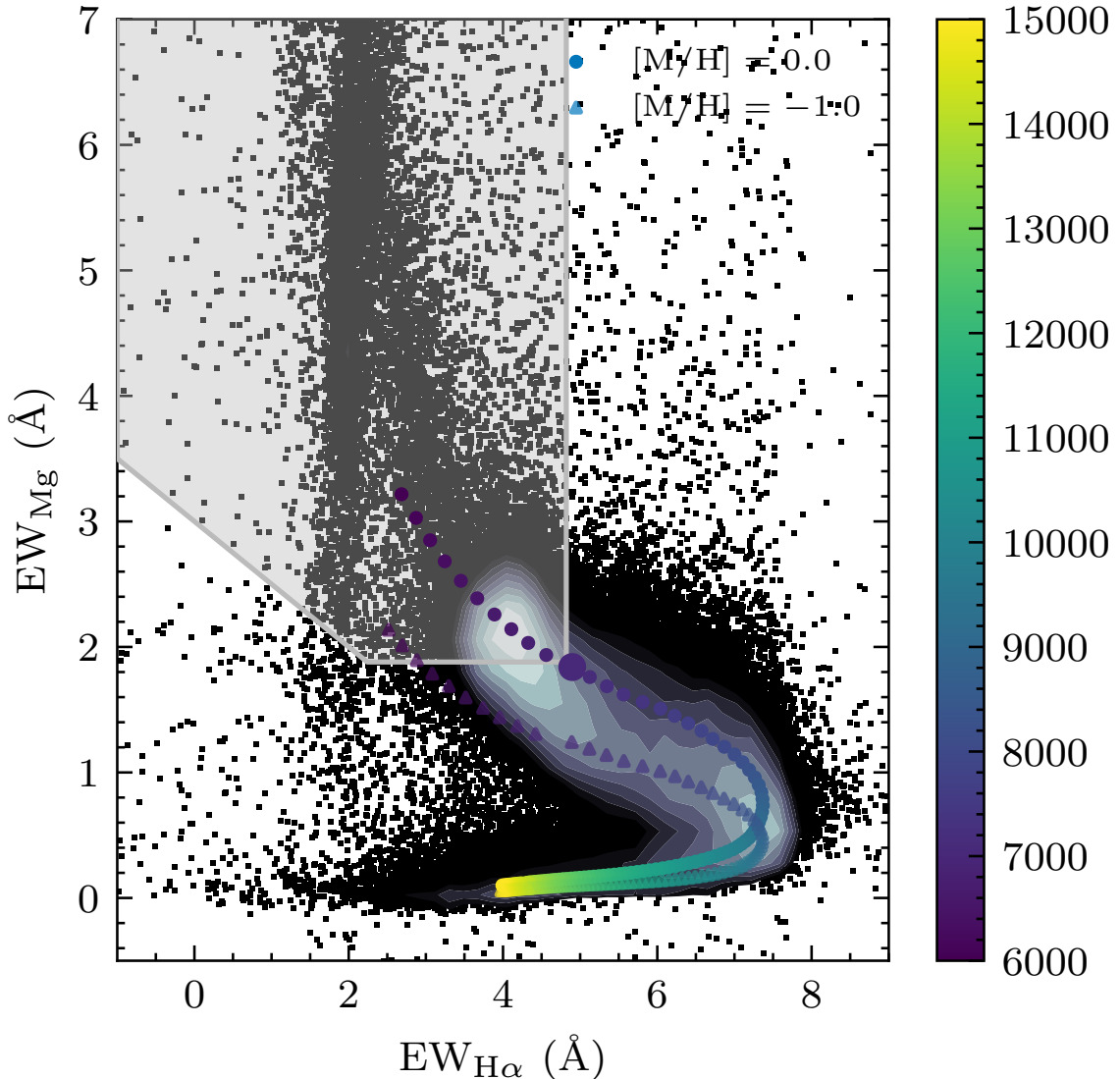


**Figure 2.** Distribution of the H $\alpha$  and Mg I  $b$  line indices of the MRS sample. Regions with high number densities are shown as grayscale contours. Reference line indices from the ATLAS atmospheric models in the range from 6000 K to 15,000 K are overplotted as colored circles ( $\log g = 4.0$  dex,  $[M/H] = 0.0$  dex) and triangles ( $\log g = 4.0$  dex,  $[M/H] = -1.0$  dex). The large circle at  $EW_{Mg} \sim 2$  Å represents the model for  $T_{\text{eff}} = 7000$  K. The shadowed area represents the selection boundary for stars cooler than 7000 K.

radiation fields (Przybilla et al. 2011). Alexeeva et al. (2018) presented NLTE models for the Mg I  $b$  lines, which is of importance in our sample’s context since neutral magnesium is a minority species. They found that departures from LTE are essential for stars hotter than 9000 K, potentially leading to differences in Mg abundance of several tenths of a dex. Although our method is inevitably limited by the systematic shortcomings embedded in the theoretical model spectra, this approach can perform well enough in practice (Ting et al. 2017a).

The training process involves two different SLAM models. The first model is used to convert high-resolution spectra from the model grid ( $T_{\text{eff}}$ ,  $\log g$ ,  $[Fe/H]$ ) to yield random values for these parameters within predefined ranges. The second one is used to construct mock spectra resembling the MRS spectra using synthetic spectra convolved with the rotational profile ( $v \sin i$ ) and instrumental broadening.

Note that the specific intensity profiles pertaining to the stellar atmosphere vary from center to limb. The convolution approach is an approximate representation of the rotation profile under the assumption that center-to-limb variations are negligible compared to rotation effects (Gray 2005). This approximation will cease to hold for rapid rotation, which



induces temperature and gravity inhomogeneities, leading to differences that depend on the spin axis orientation with respect to the line of sight. Such gravitational darkening effects, most notable in Be—B-type stars exhibiting Balmer-line emission (Townsend et al. 2004)—will result in an underestimation of the rotation velocities. Nevertheless, for the majority of our sample objects this effect is minor and only a small fraction of rapid rotators suffer from this systematic error. As for the limb darkening law, we adopted a fixed value for the linear limb-darkening coefficient,  $\epsilon = 0.6$ , a value typical for the range of temperatures found among our sample (Royer et al. 2002a). Wade & Rucinski (1985) pointed out that the coefficient depends on the effective temperature and the wavelength, and Díaz et al. (2011) estimated that neglecting these variations may produce an error of  $\sim 2\%$  in  $v \sin i$ ; therefore, adoption of a more adequate limb darkening law would be a potential improvement.

First, we used synthetic stellar spectra from the Pollux database (Palacios et al. 2010) to generate the training set. The model grid covered  $T_{\text{eff}}$  from 6000 K to 15,000 K in steps of 100 K,  $\log g$  from 3.5 dex to 4.5 dex in steps of 0.5 dex, and  $[\text{Fe}/\text{H}]$  from  $-1.0$  dex to 1.0 dex in steps of 0.5 dex. Spectra were computed based on the plane-parallel ATLAS12 model atmospheres in LTE (Kurucz 2005). The microturbulent velocity was fixed at  $2 \text{ km s}^{-1}$ . We used this original set of ATLAS12 model spectra to train the first SLAM model and then applied this SLAM model to generate 10,000 synthetic spectra covering a uniform distribution in  $\log(T_{\text{eff}})$ ,  $\log g$ , and  $[\text{Fe}/\text{H}]$ .

In the second step, the synthetic spectra were convolved with the rotational broadening and downgraded to a resolution of  $R \sim 7500$  to resemble the MRS spectra from both the blue and red arms. We normalized these mock spectra using the same procedure as used for the MRS spectra and re-sampled them to a wavelength step of  $0.2 \text{ \AA}$ , approximately the sampling step of  $\lambda/3R$ . Gaussian noise resulting in  $\text{SNR} = 40$  was added to the spectra to simulate the practical conditions pertaining to the observed spectra.

We adopted a grid of SLAM hyperparameters (parameters used to control the learning process) defined by  $\epsilon = 0.05$ ,  $C = [0.1, 1, 10]$ , and  $\gamma = [0.1, 1, 10]$ , where  $\epsilon$  and  $C$  represent the tube radius and penalty level in the SVR algorithm, respectively, and  $\gamma$  represents the width of the kernel of the radial basis function. These hyperparameters define the complexity of the SVR model, which is automatically determined by the training set through the mean-squared error. The best-fitting hyperparameters were found through five-fold cross-validation, i.e. by partitioning the entire training sample into five equal-sized subsets and adopting a single subsample as validation data to test the model trained by the other four subsamples. This cross-validation was repeated five times, iterating through all five subsamples.

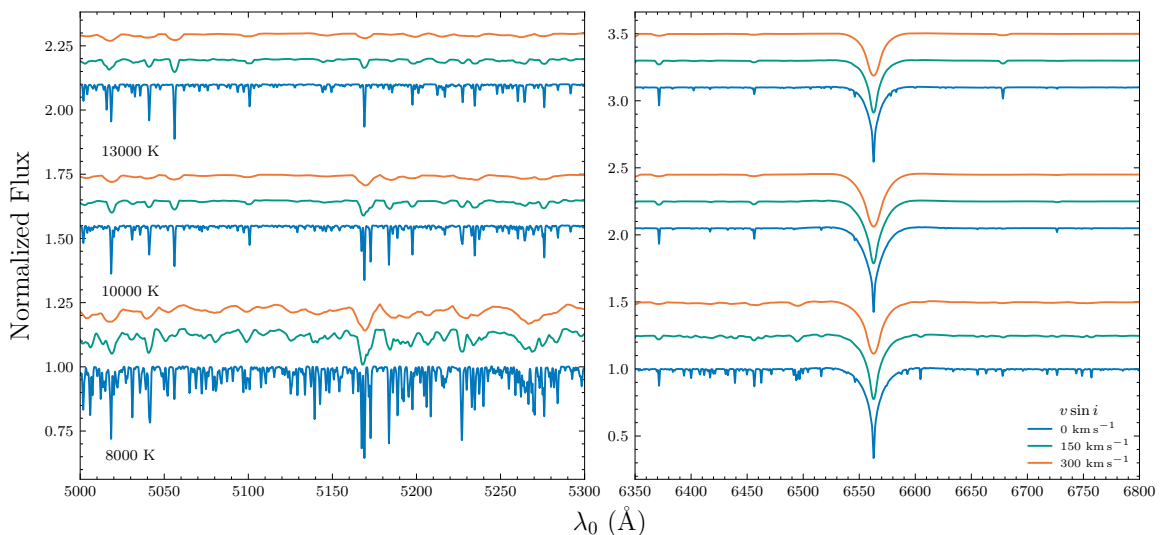


**Figure 3.** Model spectra for  $T_{\text{eff}} = 8000 \text{ K}$  (bottom),  $10000 \text{ K}$  (middle), and  $13000 \text{ K}$  (top). Each group is further offset by  $v \sin i = 0 \text{ km s}^{-1}$  (blue),  $150 \text{ km s}^{-1}$  (green), and  $300 \text{ km s}^{-1}$  (orange). Observations of the same object obtained with the blue and red arms are shown in the left and right panels, respectively. The model spectra have been broadened to the MRS resolving power,  $R = 7500$ , and resampled to the MRS wavelength coverage.

The predicted performance of the SLAM method fundamentally depends on how the spectral-line features vary as a function of the adopted labels. As one of the first applications to early-type stars, we present Figures 3, 4, and 5 to illustrate these variations as functions of  $v \sin i$ ,  $[\text{M}/\text{H}]$ , and  $\log g$ , respectively. Three groups of model spectra

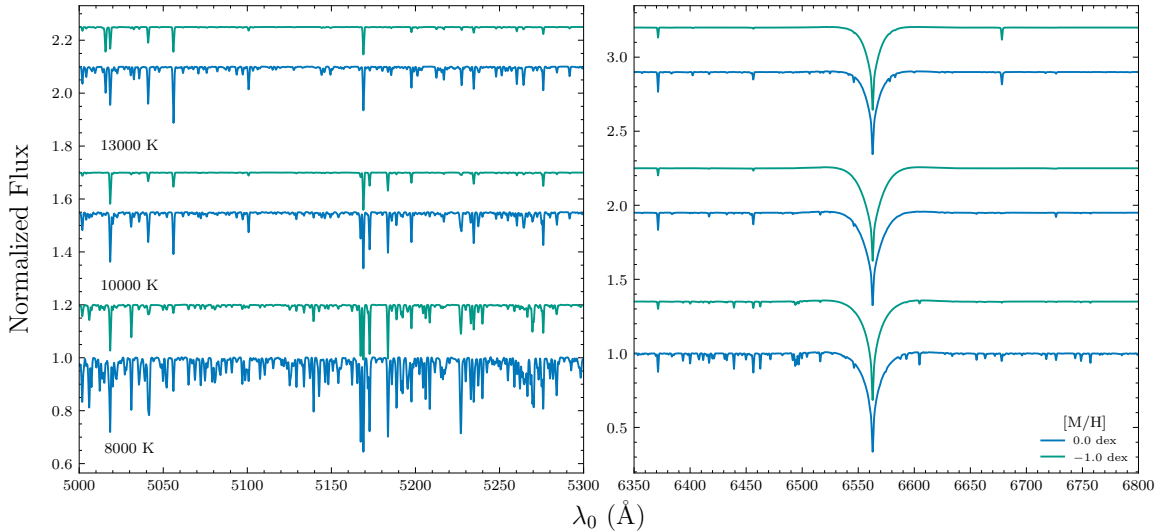


**Figure 4.** As Figure 3, but for different metallicities, i.e.,  $[M/H] = 0.0$  dex (blue) and  $-1.0$  dex (green).

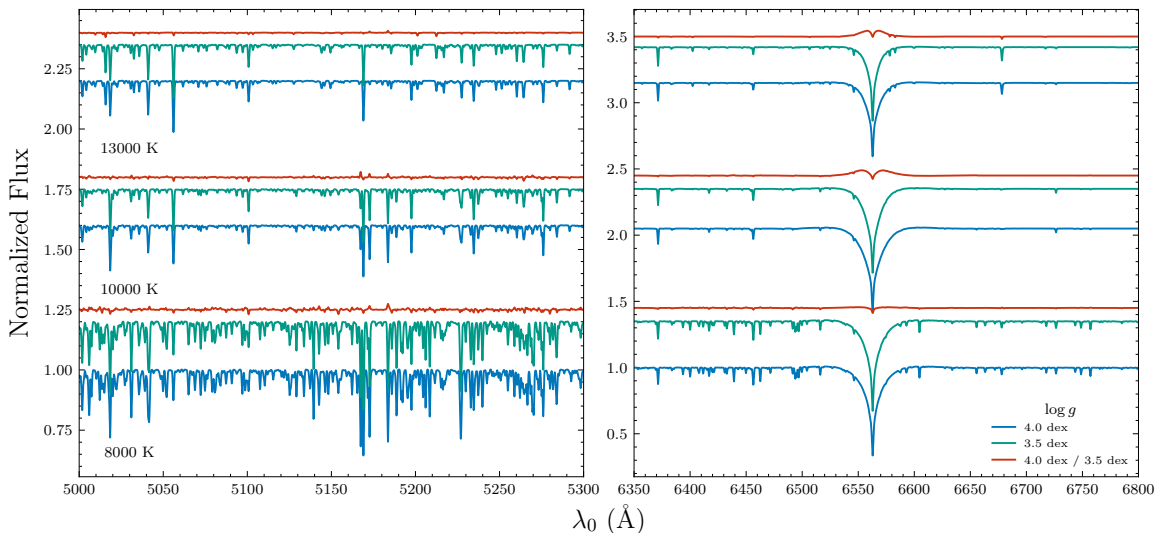


**Figure 5.** As Figure 3, but for different surface gravities, i.e.,  $\log g = 4.0$  dex (blue) and  $3.5$  dex (green). The red curve represents the flux ratio of the  $\log g = 4.0$  dex and  $\log g = 3.5$  dex models,  $F_{\log g=4.0}/F_{\log g=3.5}$ .

for different temperatures are shown at the top (13,000 K), middle (10,000 K), and bottom (8000 K). The left (right) panels show the blue (red) segments of the MRS spectral range. The model spectra were broadened to the MRS resolving power,  $R = 7500$ , and resampled to the MRS wavelength coverage. The default parameter set includes solar metallicity  $[M/H] = 0$ ,  $\log g = 4.0$  dex, and  $v \sin i = 0 \text{ km s}^{-1}$ .

Figure 3 and 4 show clear evidence that the model spectra are strongly dependent on the values of  $v \sin i$  and  $[M/H]$ . As the rotation velocity increases, the absorption lines become blended and only strong lines remain visible. The effects of rotational broadening on the spectra can be differentiated easily from the impact of other stellar labels ( $T_{\text{eff}}$ ,  $[M/H]$ , and  $\log g$ ). This enables us to unequivocally probe the effects of stellar rotation. All metal line depths decrease with decreasing metallicity, although the  $H\alpha$  profile is largely unchanged (as is He I 6678 for hotter B-type stars). Thus, the potential degeneracy between higher temperature and lower metallicity could be alleviated by the strength of the  $H\alpha$  profile. Moreover, the equivalent widths of the Balmer lines are maximal around 9000 K due to the relatively high excitation energy of the Balmer series (10.2 eV) (Gray 2005). The presence of He I and/or Si II, which only appear at higher temperatures, could help to resolve this degeneracy.

Any variations caused by variations in  $\log g$  are small, as shown in Figure 5. To provide to a clearer picture of the latter effect, the flux ratios of the  $\log g = 4.0$  dex and  $\log g = 3.5$  dex models,  $F_{\log g=4.0}/F_{\log g=3.5}$ , are overplotted as red curves. Generally, the dependence on  $\log g$  is weak. In the blue arm, mostly only the Mg I *b* lines exhibit some changes for cooler models. As for H $\alpha$  in the red arms, its wings are merely influenced by Stark broadening for the hotter models with lower gravity, and only the line cores show some dependence on  $\log g$ . This suggests a poor capability for predicting the surface gravity, particularly for cooler stars.

### 3.2. Uncertainties

We will discuss two types of uncertainties, internal errors associated with the SLAM method itself and external uncertainties associated with the observed spectra.

The internal uncertainty pertaining to the optimization method could be represented by the SLAM errors, as converted from the Hessian matrix. The diagonal elements of the covariance matrix were used as the formal errors. We also estimated the precision of the model based on the cross-validated scatter ( $\sigma_{CV}$ ), which is the standard deviation of the difference between the predicted and true values:

$$\sigma_{CV} = \frac{1}{m} \sqrt{\sum_{i=1}^m (\theta_{i,SLAM} - \theta_i)^2}, \quad (2)$$

where  $\theta_i$  and  $\theta_{i,SLAM}$  are the true and predicted stellar labels, respectively. The cross-validated scatter was calculated based on a subset composed of one-tenth of the full training sample. This subset was randomly selected to ensure uniformity across the parameter ranges.

Figure 6 shows the uncertainties in the stellar labels for different SNRs, from 20 to 100. For objects with  $SNR > 60$ , the  $\sigma_{CV}$  values for  $T_{eff}$ ,  $\log g$ ,  $[M/H]$ , and  $v \sin i$  are  $\sim 75$  K, 0.06 dex, 0.05 dex, and  $\sim 3.5$  km s $^{-1}$ , respectively. Both  $\sigma_{CV}$  and the SLAM error converge for  $SNR > 60$ , but  $\sigma_{CV}$  is much larger than the SLAM error. This is due to the unconsidered errors in the stellar labels in both the training and validation processes. Thus, following Zhang et al. (2020a), we recommend the cross-validated scatter as a more reliable estimate to evaluate the performance of the SLAM model. The cross-validated test also yields the biases (see the triangles in Figure 6), which contribute less than 10% to the overall uncertainties.

Note that the uncertainties just discussed represent the average behavior of the SLAM model. Its performance will vary across a wide range of the relevant parameter space, especially for  $T_{eff}$ . The top left panel of Figure 6 shows  $\sigma_{CV}$  for two different subsamples, divided by their temperatures,  $T_{eff} < 10,000$  K (dashed line) and  $T_{eff} > 10,000$  K (dotted line). The performance of the hotter subsample is much worse than that of the cooler stars. The same trend with effective temperature is seen for  $[M/H]$  and  $v \sin i$ . Figure 3 shows that the available metallic absorption features become weaker as the temperature increases, particularly for the blue arm. This lack of information leads to larger uncertainties in estimates of the stellar labels for hotter stars, which also holds for lower metallicities. The exception is  $\log g$  (top right), where there is no significant difference between the  $\sigma_{CV}$  values for the hotter and cooler subsamples. This could be due to our use of both the blue and red segments of the MRS spectra, which broadly offsets the spectral dependence on effective temperature.

### 3.3. Validation

A comparison of the stellar labels derived from SLAM and those collected from the literature is shown in Figure 7. The validation sample comes from Huang & Gies (2006a,b), Huang et al. (2010), Zorec & Royer (2012), and Soubiran et al. (2016). Soubiran et al. (2016) is a bibliographical catalog containing determinations of stellar atmospheric parameters. Its stellar parameters ( $T_{eff}$ ,  $\log g$ , and  $[M/H]$ ) were collected from the literature based on high-resolution ( $R \geq 25,000$ ) and high SNR ( $SNR > 50$ ) spectra. Although these parameters were not derived homogeneously, the median value of the standard deviation of the values from different measures is 0.76%. The main sources of rotational velocities are Huang & Gies (2006b) and Huang et al. (2010). Those authors conducted a survey of B-type stars based on moderate-resolution ( $R \sim 2000$ – $4000$ ) spectra from the WIYN 3.5 m and CTIO 4 m telescopes.

The top left panel of Figure 7 presents a comparison of the effective temperatures. Because Zorec & Royer (2012) estimated their temperatures based on Strömgren photometric color indices, which is inconsistent with the spectroscopic method used for our sample and other literature sources, we did not include their estimates. There is great consistency between our results and the literature results up to  $T_{eff} = 15,000$  K. This is the temperature limit inherited from the



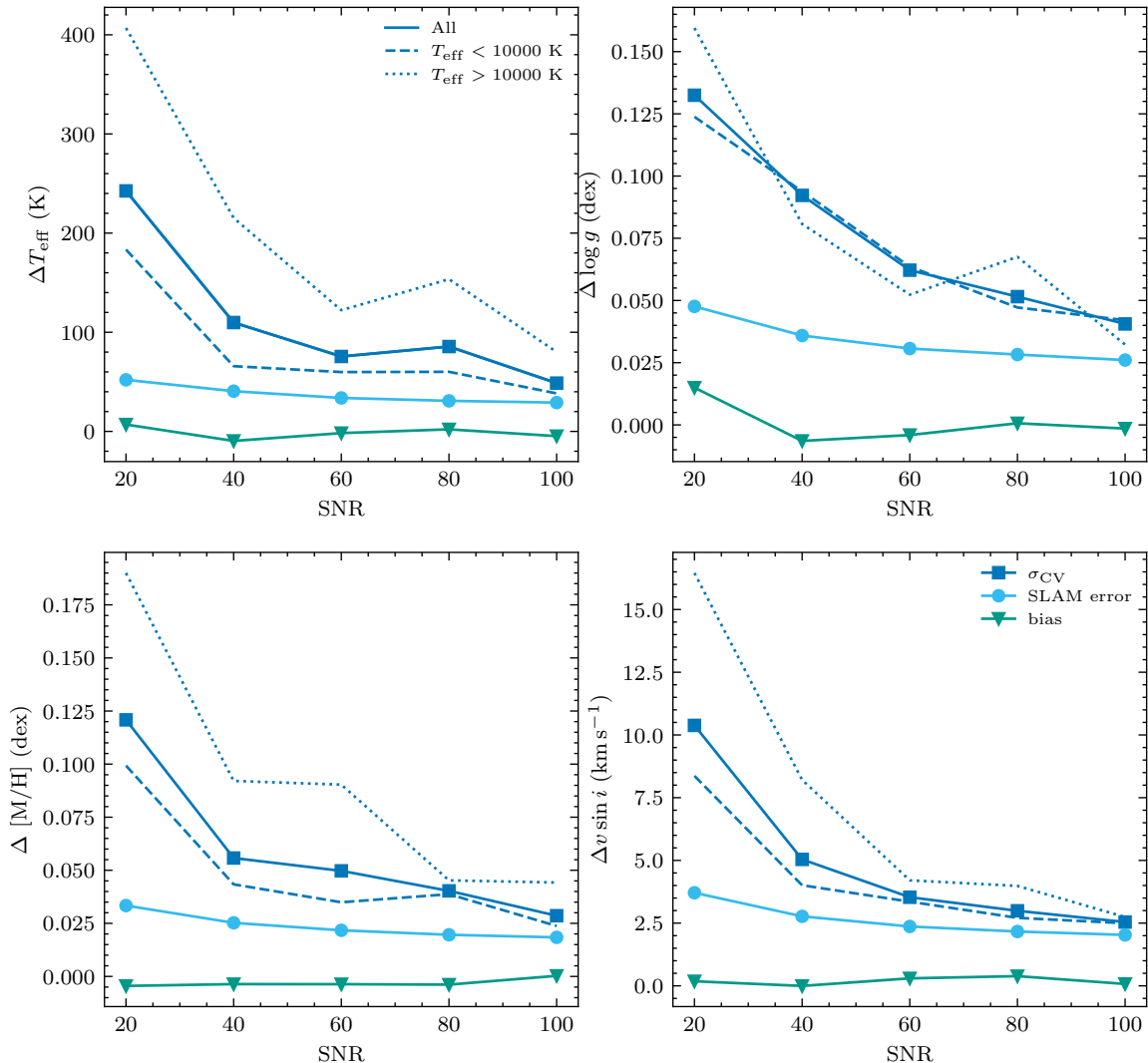


**Figure 6.** Uncertainties in the stellar labels ( $T_{\text{eff}}$ ,  $\log g$ ,  $[M/H]$ , and  $v \sin i$ ) versus SNR. Blue squares, cyan circles, and green triangles represent the cross-validated scatter,  $\sigma_{\text{CV}}$ , SLAM error, and bias, respectively. The  $\sigma_{\text{CV}}$  values of  $T_{\text{eff}}$ ,  $\log g$ ,  $[M/H]$ , and  $v \sin i$  mostly converge at  $\sim 75$  K, 0.06 dex, 0.05 dex, and  $\sim 3.5$   $\text{km s}^{-1}$ , respectively, for SNR  $> 60$ . In each panel, the  $\sigma_{\text{CV}}$  values of the corresponding label for two different subsamples, split by their temperatures, are shown as dashed ( $T_{\text{eff}} < 10,000$  K) and dotted ( $T_{\text{eff}} > 10,000$  K) lines.

training model, where the upper limit is set by the parameter grid of the atmospheric models. Thus, we disregard  $T_{\text{eff}}$  comparisons beyond this limit.

As for  $\log g$  (see the top right panel of Figure 7), it demonstrates the worst performance among the four stellar labels:  $\log g$  from SLAM roughly agrees with the literature values, although with significant scatter. This poor performance of  $\log g$  has been investigated by Zhang et al. (2020b), who used the Coefficient of Dependence (COD) to quantify the global spectral information content. They found that the COD of  $\log g$  remains low for dwarf stars. This means that the spectral information content in  $\log g$  is not well carried in the MRS spectra. This is, however, not a major issue for our analysis as the resulting  $v \sin i$  values are not significantly affected by this poor performance (as demonstrated in the bottom right panel of Figure 7). Our analysis of the bolometric luminosities (see Section 4.1) and, thus, the stellar masses (see Section 4.2) depends only weakly on this stellar label.

$[M/H]$  from SLAM follows the one-to-one correlation with the literature results. However, there might be an offset of 0.08 dex toward higher metallicity. This might be due to the intrinsic error in the training model. However, the linear correlation with a slope close to unity ensures the reliability of our estimates.

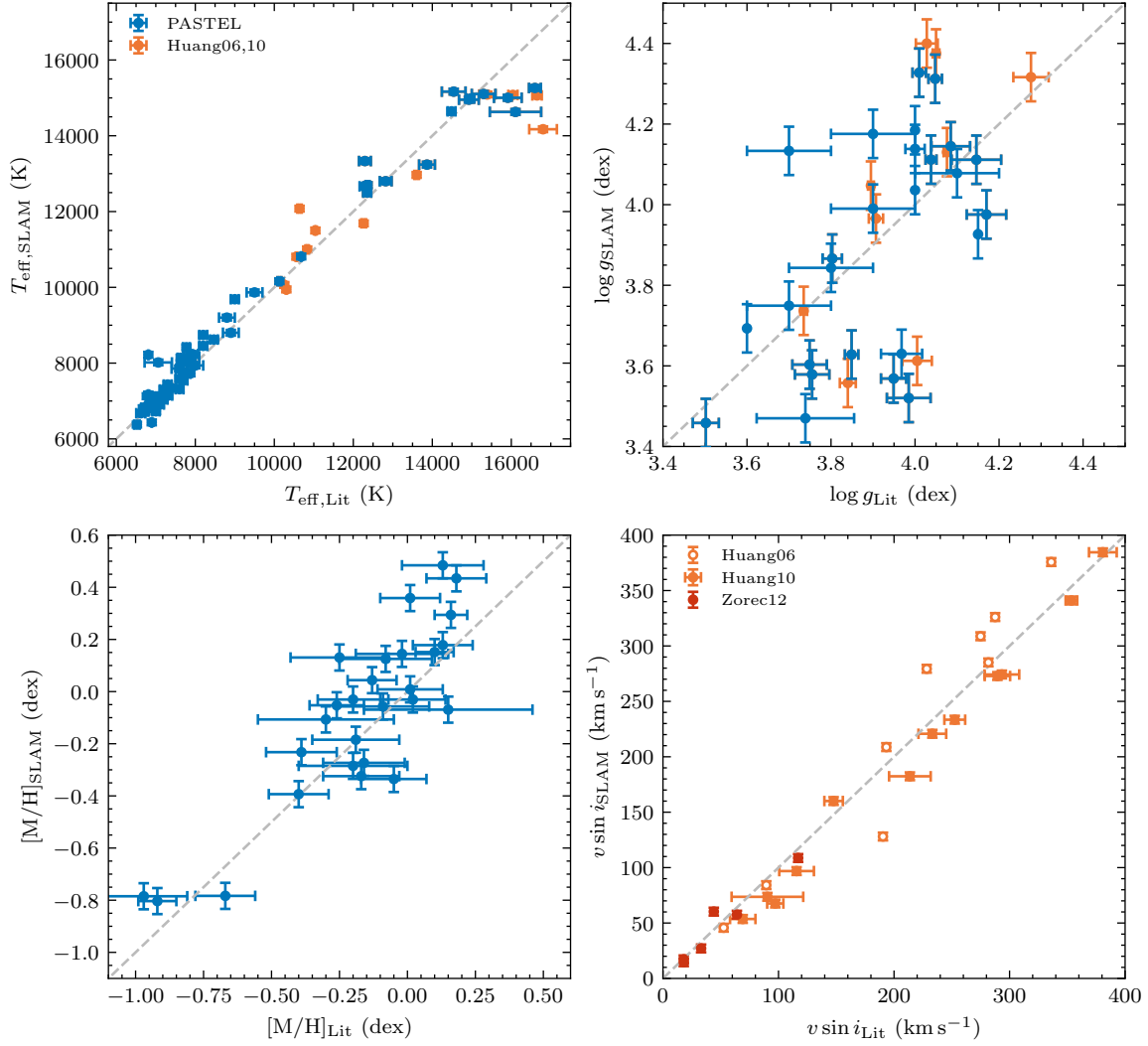


**Figure 7.** Comparison of stellar labels from SLAM and literature results (Huang & Gies 2006a,b; Huang et al. 2010; Zorec & Royer 2012; Soubiran et al. 2016). (Top left)  $T_{\text{eff}}$  shows great consistency for  $T_{\text{eff}} < 15,000$  K, the upper limit from the training model. The vertical error bars are on the order of or smaller than the data points. (Top right)  $\log g$  from SLAM marginally agrees with the literature values, with significant scatter. (Bottom left)  $[M/H]$  from SLAM follows the one-to-one correlation with the literature results. (Bottom right) Our estimates of  $v \sin i$  are consistent with the one-to-one relation with the literature values. The  $v \sin i$  values from Huang & Gies (2006a) and Huang et al. (2010) were calibrated based on high-precision measurements. The error bars for our estimates (horizontal axis) come from the cross-validated scatter ( $\sigma_{CV}$ ).

The bottom right panel of Figure 7 presents a comparison of  $v \sin i$  values. Despite their low resolution ( $R \sim 2000$ – $4000$ ), Huang & Gies (2006a) and Huang et al. (2010) achieved sufficient SNR ( $> 50$ ) to ensure the reliability of their measurements. Their results have been validated by Zorec & Royer (2012), yielding an almost one-to-one correlation (with a slope of  $0.971 \pm 0.04$ ) with the results from high-resolution ( $R > 20,000$ ) spectra. For the  $v \sin i$  comparison, we used the calibration function derived by Zorec & Royer (2012, their Equation 3) to correct their values. Zorec & Royer (2012) compiled the current-largest catalog of 1014 A-type field stars, which includes Royer et al. (2002a,b)’s results. However, because our sample is on average  $\sim 4$  mag fainter than theirs, there are only six matches (included in Figure 7). Linear regression yields,

$$v \sin i_{\text{SLAM}} = 1.05_{\pm 0.04} v \sin i_{\text{Lit}} - 4.97_{\pm 8.37}, \quad (3)$$

which is a remarkable consistency in measures of  $v \sin i$ . The offset is not significant compared with its uncertainty, which could be associated with the variable instrumental broadening. The actual spectral resolution of a fiber depends

on its location on the observation plate, which may generate slightly different broadening values. The wavelength coverage of a given spectrum is also affected by the fiber positioning, leading to variations in the information retained in the data. Both effects introduce possible biases in estimates of stellar rotation, but they are well-constrained in the slow rotation regime.

Ideally, rotation measurements should be linked to surface gravity measurements, in the sense that the surface gravity determines the steepness of the pressure gradient, which in turn generates the pressure broadening, a second broadening mechanism in addition to the rotational instrumental broadening. The uncertainties in estimating  $\log g$  should therefore affect the  $v \sin i$  derivation. In our case, this effect could be mediated in one of three ways. First, pressure broadening strongly affects predominantly the Balmer lines rather than the narrow lines (e.g. Mg I  $b$ ); rotational information is well preserved if one were to use narrow-line absorption. Second, the median-resolution spectrograph enables us to resolve the different broadened rotation and pressure profiles. Using a method similar to profile fitting rather than calculating the full width at half maximum, we can disentangle these two mechanisms. Third, the vast majority of our sample objects are dwarf stars. They span a relatively small range in  $\log g$ , around 4.0 dex, compared with the giant stars. Thus, the impact of large uncertainties in  $\log g$  can be controlled adequately.

Moreover, the consistency between our estimates and the literature results can extend to lower  $v \sin i$ , even below the detection limit for MRS resolution, suggesting that our estimates can potentially apply also to very slow rotators. Since the offset (if any) is minor, we used the results from the SLAM model without adjustments. For further use of complementary samples, we recommend using the inverse function of Equation 3 for calibration.

## 4. RESULTS

Here we discuss our procedures to derive the fundamental parameters (bolometric luminosity, mass, and age) from the SLAM stellar labels, including the extinction and bolometric corrections (Section 4.1), and the use of the stellar evolutionary diagram (Section 4.2). We further demonstrate the impact of our selection criteria on these fundamental parameters, as well as the stellar labels, allowing us to derive the final catalog.

### 4.1. Bolometric luminosities

Since the majority of our sample is embedded in the Galactic disk, we use the high-precision photometry from *Gaia*, combined with 2MASS photometry given that it is only marginally affected by extinction, to estimate the bolometric luminosities. We infer the extinction toward each star based on the difference between the observed *Gaia* and the intrinsic color indices. The intrinsic color index,  $(G_{\text{BP}} - G_{\text{RP}})_0$ , was derived from the PARSEC 1.2S (Bressan et al. 2012) evolutionary tracks by interpolating the model grid defined by  $\log T_{\text{eff}}$ ,  $\log g$ , and  $[M/H]$  (assuming no  $\alpha$  enhancement) to the corresponding values derived from SLAM.

The typical uncertainty in  $E(G_{\text{BP}} - G_{\text{RP}})$  should be on the order of 0.1 mag (e.g. Green et al. 2019). Figure 8 shows a comparison of  $E(B - V)$  values estimated in this paper and by Green et al. (2019). The transformation from measured  $E(G_{\text{BP}} - G_{\text{RP}})$  to  $E(B - V)$  was calculated based on the Cardelli et al. (1989) and O'Donnell (1994) extinction law with  $R_V = 3.1$ . The extinction from Green et al. (2019) was queried based on dust maps (Green 2018) and converted to  $E(B - V)_{\text{Green}}$  using Table 6 of Schlafly & Finkbeiner (2011).

Since our sample stars are mostly embedded in the Galactic disk, we selected two subsamples affected by significant reddening, i.e.  $E(B - V) > 0.5$  mag and  $0.25$  mag  $< E(B - V) < 0.5$  mag. Comparison with the Green et al. (2019) reddening map for high extinction suggests a typical uncertainty of  $\sim 0.1$  mag in  $E(B - V)$ . There is great consistency between both estimates, although our results might be biased toward lower extinction by  $\sim 0.01$  mag.

The bolometric correction (BC) was adopted from Chen et al. (2019), who considered the effects of spectral type and non-linearities. The bolometric luminosities were calculated as

$$M_{\text{bol}} = m_{K_s} + BC_{K_s} - DM - \frac{A_{K_s}}{E(G_{\text{BP}} - G_{\text{RP}})} E(G_{\text{BP}} - G_{\text{RP}}), \quad (4)$$

where DM is the distance modulus calculated from the *Gaia* EDR3 parallaxes (Bailer-Jones et al. 2021) and  $A_i$  is the extinction coefficient for a given passband,  $i$ , based on O'Donnell (1994). We adopted the 2MASS  $K_s$  band to mitigate the influence of extinction in the Galactic plane. Since the photometric precision of the 2MASS  $K_s$  band is better than 0.03 mag for our sample (Skrutskie et al. 2006) and infrared bands are less affected by extinction ( $\frac{A_{K_s}}{E(G_{\text{BP}} - G_{\text{RP}})} = 0.26$ ), the choice of  $K_s$  leads to better estimates of  $M_{\text{bol}}$ . The bolometric luminosities were derived by adopting  $M_{\odot, \text{bol}} = 4.74$  mag. The corresponding error was estimated by bootstrap sampling of all determinations

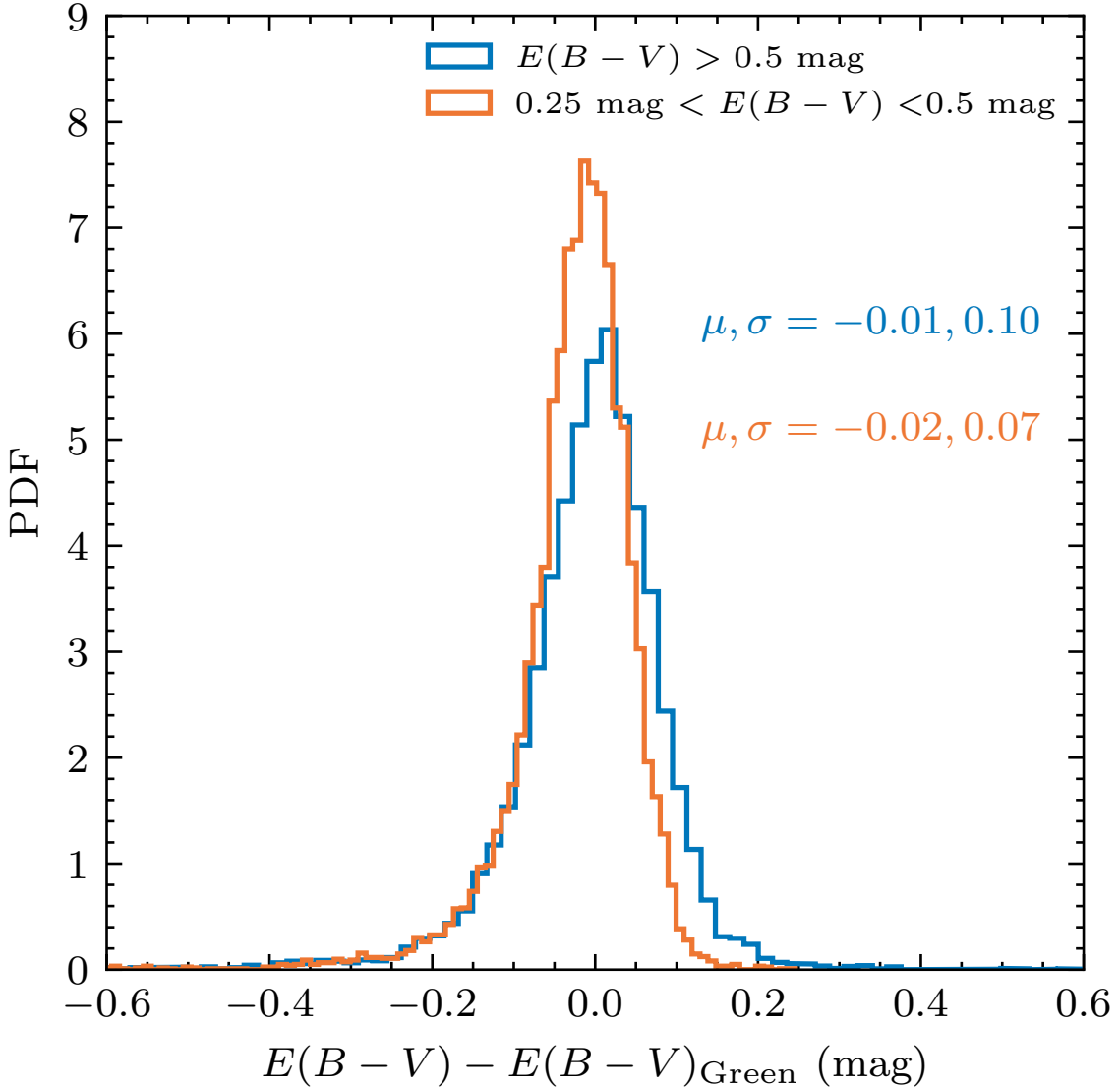


**Figure 8.** Distribution of the difference in  $E(B - V)$  estimated in this paper and by Green et al. (2019). The comparisons are for stars with  $E(B - V) > 0.5$  mag (blue) and  $0.25 \text{ mag} < E(B - V) < 0.5$  mag (orange). The mean values of the differences ( $\mu$ ) and the dispersions ( $\sigma$ ) are also shown.

using Equation 4, including the stellar labels. The median value of the uncertainties in the bolometric luminosities is  $\Delta \log(L/L_{\odot}) = 0.02$ .

We show the Hertzsprung–Russell diagram of our sample objects in Figure 9. The majority of the sample have effective temperatures between 6500 K and 15,000 K. The lower boundary reflects the rejection of stars with  $T_{\text{eff}} < 6500 \text{ K}$ — $\log(T_{\text{eff}}/\text{K}) < 3.81$ —in Section 2.1, whereas the upper boundary is limited by the hottest stars in the ATLAS atmospheric models. Note that there is an abnormal concentration close to the 15,000 K boundary. This is an artifact caused by the temperature limit in the training process. Thus, we reject all stars with  $T_{\text{eff}} > 14,500 \text{ K}$ — $\log(T_{\text{eff}}/\text{K}) > 4.16$ —(black vertical line) from further analysis. The aggregation around 9400 K— $\log(T_{\text{eff}}/\text{K}) \sim 3.97$ —shown in Figure 2 no longer exists, suggesting that it does not reflect any real physical property.

In addition to a temperature cut, we also limited our selection to those stars that are still on the main sequence. As stars evolve off the core-hydrogen-burning phase, their rotation velocities decelerate significantly owing to the conservation of angular momentum during the evolutionary expansion of subgiant-branch stars (e.g., Wu et al. 2016). Because these evolved stars may have  $\log g$  beyond our model grids, we cannot confirm the accuracy of any resulting

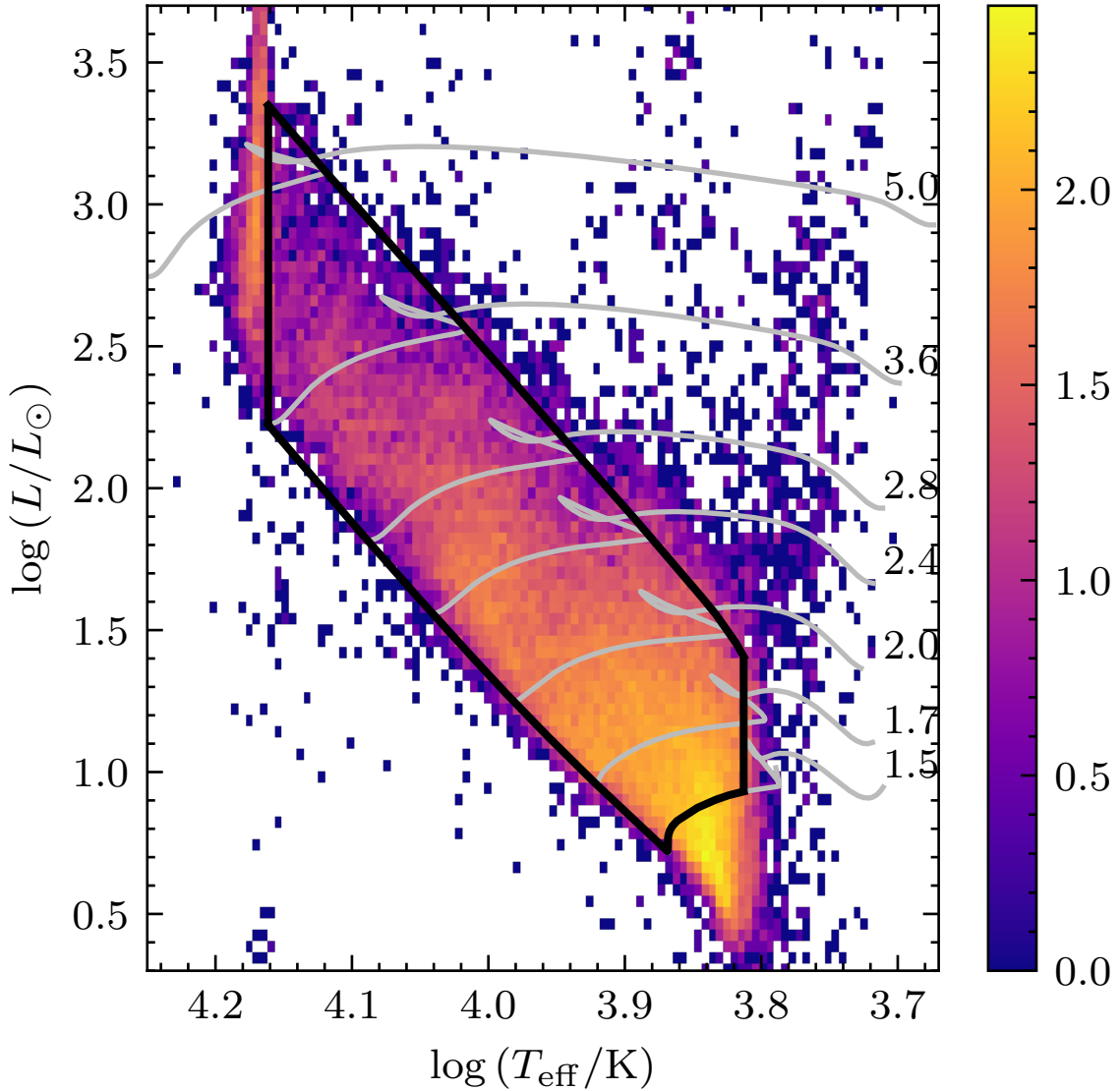


**Figure 9.** Hertzsprung–Russell diagram of single, normal stars. Evolutionary tracks of 1.5, 1.7, 2.0, 2.4, 2.8, 3.6, 5  $M_{\odot}$  are shown as gray curves. Black reference lines outline the selection boundary for stars of solar metallicity. The colors represent the logarithm of the stellar numbers in each bin.

estimates. Our selection boundary also includes some stars in the small contraction phase before they move toward the red giant branch. This phase is a rapid transition from core to shell hydrogen burning. Therefore, any contamination associated with this phase will be of minor importance.

#### 4.2. Stellar masses and ages

We used PARSEC 1.2S evolutionary tracks in the  $\log T_{\text{eff}}\text{--}\log L$  space to estimate individual stellar masses and ages for a given metallicity,  $[M/H]$ . Following Zorec & Royer (2012), we represent the stellar age by  $t$ , for the age in years, as well as by  $t/t_{\text{MS}}$ , for the life span from the ZAMS to the terminal-age main sequence (TAMS). The corresponding error was estimated by resampling of  $\log T_{\text{eff}}$  and  $\log L$ . Figure 9 shows that parts of the evolutionary tracks of the shell H-burning phase reside within our selection boundary for main-sequence stars, generating a degeneracy between mass and age. In order to test its influence on our approach, we performed the same analysis on a mock data set, extracted from theoretical evolutionary tracks. We verified that the degeneracy is only important for objects at the very end of the evolutionary phase ( $t/t_{\text{MS}} > 0.95$ ). The corresponding error is smaller than 2% for both the resulting mass and age estimates.



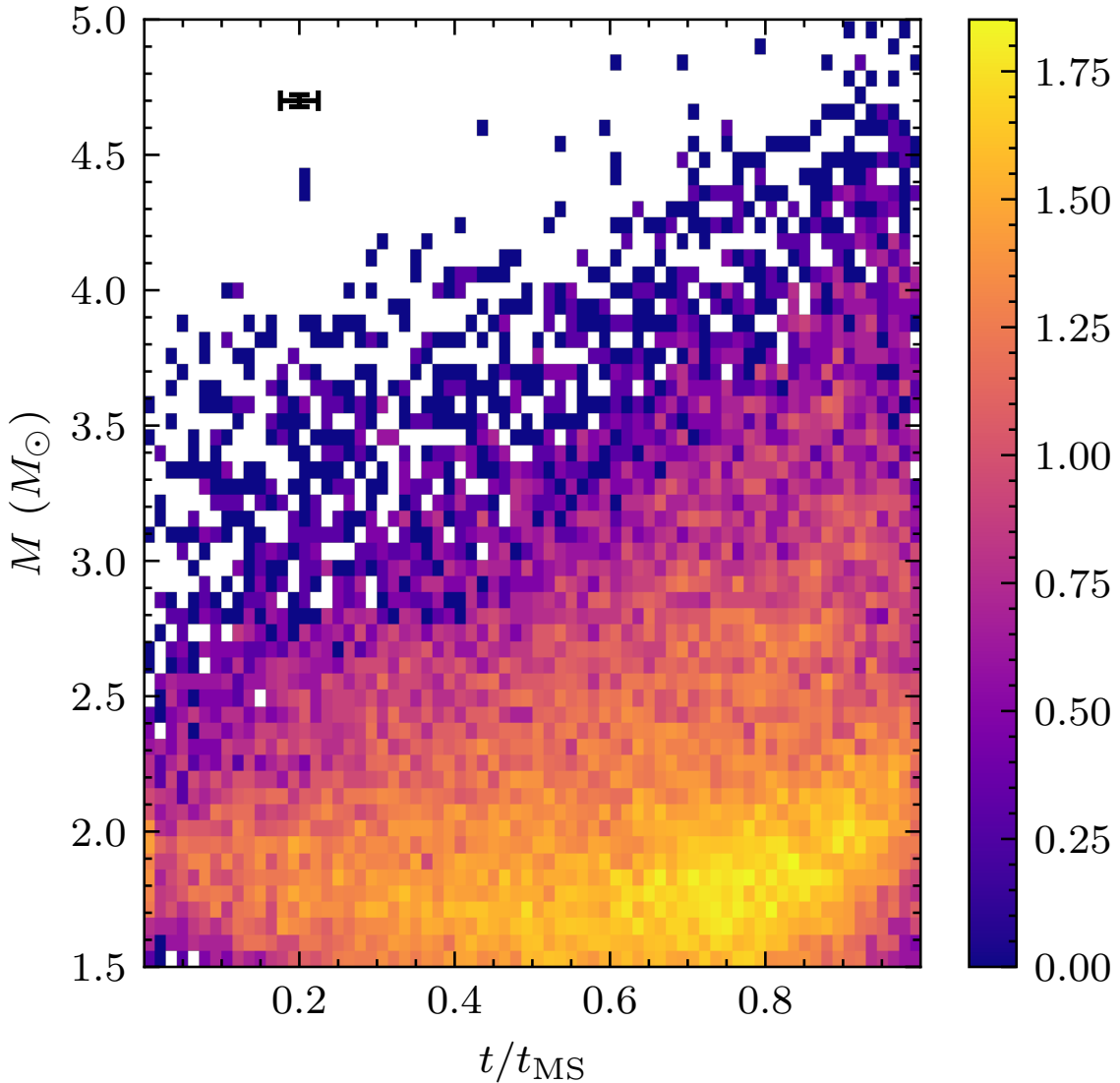


**Figure 10.** Mass and age ( $t/t_{\text{MS}}$ ) distributions of selected single, normal stars. Typical errors are indicated by the error bar at top left.

In Figure 10, we present the distribution in the  $t/t_{\text{MS}}-M$  plane of the single, normal stars selected within the boundary defined in Figure 9. The general distribution of our sample in the mass–age diagram displays a similar profile as that of Zorec & Royer (2012). The trend toward larger  $t/t_{\text{MS}}$  with increasing mass reflects the temperature cut at  $T_{\text{eff}} = 14500$  K (the vertical line in Figure 9). However, our sample fills the lack of objects observed for the lower mass regime (their Figure 4).

Fast rotators ( $v \sin i > 300 \text{ km s}^{-1}$ ) will change their surface temperatures and luminosities significantly compared with their non-rotating counterparts. This is mainly due to (1) the notion that the centrifugal support results in a decrease in the surface temperature and luminosity by decreasing the effective gravity (Meynet & Maeder 1997); and (2) the orientation of a star with respect to the line of sight determines the observed fraction of the stellar surface (Collins & Smith 1985). Such mechanisms are not included in the Bressan et al. (2012) non-rotating evolutionary tracks and might introduce additional biases and uncertainties into estimates of fundamental stellar parameters. This caveat could be alleviated by employing detailed asteroseismic modeling (e.g. Corsaro et al. 2017; Li et al. 2019). Unfortunately, such information is not available for our sample. Nevertheless, parameters based on non-rotating models are slightly influenced by rotation effects. Zorec & Royer (2012) compared the masses and ages determined based on non-rotating evolutionary tracks with those resulting from rotation (Meynet & Maeder 2000; Ekström et al. 2008; Brott et al. 2011;

**Table 1.** Contents of the Catalog

Num	Column	Unit	Description
1	ID		<i>Gaia</i> DR3 source ID
2	obsid		LAMOST MRS observation ID
3	RA	°	Right Ascension (J2000)
4	Dec	°	Declination (J2000)
5, 6	EW <sub>H<math>\alpha</math></sub> , EW <sub>Mg</sub>	Å	Line indices of H $\alpha$ and Mg I <i>b</i> EW
7, 8	$v_{R,b}$ , $v_{R,r}$	km s <sup>-1</sup>	Radial velocities, blue and red arms
9	$T_{\text{eff}}$	K	Effective temperature from SLAM
10	$\sigma_{T_{\text{eff}}}$	K	Uncertainty in $T_{\text{eff}}$ (SLAM error)
11	$\log g$	dex	Surface gravity from SLAM
12	$\sigma_{\log g}$	dex	Uncertainty in $\log g$ (SLAM error)
13	[M/H]	dex	Metallicity from SLAM
14	$\sigma_{\text{[M/H]}}$	dex	Uncertainty in [M/H] (SLAM error)
15	$v \sin i$	km s <sup>-1</sup>	Projected rotation velocity from SLAM
16	$\sigma_{v \sin i}$	km s <sup>-1</sup>	Uncertainty in $v \sin i$ (SLAM error)
17	$\log L/L_{\odot}$		Logarithmic luminosity
18	$\sigma_{\log L}$		Uncertainty in $\log L/L_{\odot}$
19	$M$	$M_{\odot}$	Stellar mass
20	$\sigma_M$	$M_{\odot}$	Uncertainty in $M$
21	$t/t_{\text{MS}}$		Life span from the ZAMS to the TAMS
22	$\sigma_{t/t_{\text{MS}}}$		Uncertainty in $t/t_{\text{MS}}$
23, 24	SNR <sub>b</sub> , SNR <sub>r</sub>		Signal-to-noise ratio for blue and red arms
25, 26	$\chi_b^2$ , $\chi_r^2$		$\chi^2$ estimates of the best fit of the blue and red arms

(Only a portion of this table is shown here to demonstrate its form and content. This table is available in its entirety in machine-readable form in the online journal.)

Ekström et al. 2012). They found that differences are smaller than or around 10% if the rotation is not close to the critical rotation rate ( $\Omega/\Omega_{\text{crit}}$ , where  $\Omega$  is the angular rotation velocity). Since only a fraction of our sample objects are rapid rotators, our implementation of non-rotating evolutionary tracks is reasonable.

As our final selection step, we discarded any star with large errors in either mass or relative age ( $\sigma_M \geq 0.1 M_{\odot}$ ,  $\sigma_{t/t_{\text{MS}}} \geq 0.15$ ). To ensure the accuracy of our  $v \sin i$  estimates, we also made a selection based on the associated SLAM error ( $\sigma_{v \sin i}/v \sin i < 0.05$ ). Combined with our temperature selection (Section 4.1), the final catalog contains 40,034 stars. All stellar labels and fundamental parameters are listed in Table 1.

## 5. CONCLUSIONS

We have compiled a spectroscopic catalog of stellar parameters for 40,034 early-type stars with  $7000 \text{ K} \leq T_{\text{eff}} \leq 14,500 \text{ K}$ . The primary selection of the LAMOST DR7 MRS spectra was carried out by considering the line indices of H $\alpha$  and Mg I *b*. We used a synthetic atmospheric model library to build the training set for a data-driven model to estimate the stellar labels. The precisions of our estimates are  $\sim 75 \text{ K}$ ,  $0.06 \text{ dex}$ ,  $0.05 \text{ dex}$ , and  $\sim 3.5 \text{ km}^{-1}$  for  $T_{\text{eff}}$ ,  $\log g$ , [M/H], and  $v \sin i$ , respectively, for  $\text{SNR} > 60$ .

As the first in a series of papers aimed at exploring stellar rotation, we have illustrated the large volume of our sample and the capability of MRS spectra to sample stellar projected rotation velocities as small as a few  $\text{km s}^{-1}$ . This will help answer fundamental questions regarding the origins and characteristics of their angular momentum. Note that the rotation behavior of our sample might be subject to external effects, e.g. binary and chemically peculiar stars. Cluster members may have a different rotation distribution compared with the field (Huang & Gies 2006b; Sun et al. 2019). These extenuating factors might influence analyses of stellar rotation. We will address this issue in Paper II, where we discuss our sample's statistical properties. Further studies should quantitatively investigate rotation as a

function of stellar mass, age, metallicity, etc. Finally, a better theoretical characterization of the angular momentum of early-type stars in our sample would be beneficial to better understand how to recover the rotation distribution.

#### ACKNOWLEDGMENTS

L. D. acknowledges research support from the National Natural Science Foundation of China through grants 11633005, 11473037, and U1631102. The Guoshoujing Telescope (the Large Sky Area Multi-Object Fiber Spectroscopic Telescope; LAMOST) is a National Major Scientific Project built by the Chinese Academy of Sciences. Funding for the project has been provided by the National Development and Reform Commission. LAMOST is operated and managed by the National Astronomical Observatories, Chinese Academy of Sciences. This work has made use of data from the European Space Agency (ESA) mission *Gaia* (<https://www.cosmos.esa.int/gaia>), processed by the *Gaia* Data Processing and Analysis Consortium (DPAC; <https://www.cosmos.esa.int/web/gaia/dpac/consortium>). Funding for the DPAC has been provided by national institutions, in particular the institutions participating in the *Gaia* Multilateral Agreement.

*Facilities:* LAMOST

*Software:* PARSEC (1.2S; [Bressan et al. 2012](#)), Astropy ([Astropy Collaboration et al. 2013](#)), Matplotlib ([Hunter 2007](#)), TOPCAT ([Taylor 2005](#)), dustmaps ([Green 2018](#))

#### REFERENCES

- Alexeeva, S., Ryabchikova, T., Mashonkina, L., et al. 2018, *ApJ*, 866, 153. doi:10.3847/1538-4357/aae1a8
- Allende Prieto, C., Koesterke, L., Hubeny, I., et al. 2018, *A&A*, 618, A25. doi:10.1051/0004-6361/201732484
- Arenou, F., Luri, X., Babusiaux, C., et al. 2018, *A&A*, 616, A17. doi:10.1051/0004-6361/201833234
- Astropy Collaboration, Robitaille, T. P., Tollerud, E. J., et al. 2013, *A&A*, 558, A33. doi:10.1051/0004-6361/201322068
- Bailer-Jones, C. A. L., Rybizki, J., Fouesneau, M., et al. 2021, *AJ*, 161, 147. doi:10.3847/1538-3881/abd806
- Bressan, A., Marigo, P., Girardi, L., et al. 2012, *MNRAS*, 427, 127
- Brott, I., de Mink, S. E., Cantiello, M., et al. 2011, *A&A*, 530, A115. doi:10.1051/0004-6361/201016113
- Cardelli, J. A., Clayton, G. C., & Mathis, J. S. 1989, *ApJ*, 345, 245. doi:10.1086/167900
- Carraro, G., Sales Silva, J. V., Moni Bidin, C., et al. 2017, *AJ*, 153, 99. doi:10.3847/1538-3881/153/3/99
- Carraro, G., Vázquez, R. A., Costa, E., et al. 2010, *ApJ*, 718, 683. doi:10.1088/0004-637X/718/2/683
- Chen, Y., Girardi, L., Fu, X., et al. 2019, *A&A*, 632, A105. doi:10.1051/0004-6361/201936612
- Collins, G. W. & Smith, R. C. 1985, *MNRAS*, 213, 519. doi:10.1093/mnras/213.3.519
- Corsaro, E., Lee, Y.-N., García, R. A., et al. 2017, *Nat. Astron.*, 1, 0064. doi:10.1038/s41550-017-0064
- Cropper, M., Katz, D., Sartoretti, P., et al. 2018, *A&A*, 616, A5. doi:10.1051/0004-6361/201832763
- Cui, X.-Q., Zhao, Y.-H., Chu, Y.-Q., et al. 2012, *RAA*, 12, 1197. doi:10.1088/1674-4527/12/9/003
- Deng, L.-C., Newberg, H. J., Liu, C., et al. 2012, *RAA*, 12, 735. doi:10.1088/1674-4527/12/7/003
- Duchêne, G. & Kraus, A. 2013, *ARA&A*, 51, 269. doi:10.1146/annurev-astro-081710-102602
- Díaz, C. G., González, J. F., Levato, H., et al. 2011, *A&A*, 531, A143. doi:10.1051/0004-6361/201016386
- Eisenstein, D. J., Weinberg, D. H., Agol, E., et al. 2011, *AJ*, 142, 72. doi:10.1088/0004-6256/142/3/72
- Ekström, S., Georgy, C., Eggenberger, P., et al. 2012, *A&A*, 537, A146. doi:10.1051/0004-6361/201117751
- Ekström, S., Meynet, G., Maeder, A., et al. 2008, *A&A*, 478, 467. doi:10.1051/0004-6361:20078095
- Gaia Collaboration, Brown, A. G. A., Vallenari, A., et al. 2018, *A&A*, 616, A1
- Gaia Collaboration, Brown, A. G. A., Vallenari, A., et al. 2021, *A&A*, 649, A1. doi:10.1051/0004-6361/202039657
- Glebocki, R., Gnacinski, P., & Stawikowski, A. 2000, *AcA*, 50, 509
- Gray, D. F. 2005, “The Observation and Analysis of Stellar Photospheres, 3rd Edition, by D.F. Gray. ISBN 0521851866, UK: Cambridge University Press, 2005.”

- Gray, R. O. & Corbally, C. 2009, *Stellar Spectral Classification by Richard O. Gray and Christopher J. Corbally*. Princeton University Press, 2009. ISBN:  $\hat{A}\hat{A}$  978-0-691-12511-4
- Green, G. M. 2018, *The Journal of Open Source Software*, 3, 695. doi:10.21105/joss.00695
- Green, G. M., Schlafly, E., Zucker, C., et al. 2019, *ApJ*, 887, 93. doi:10.3847/1538-4357/ab5362
- Gulliver, A. F. 1977, *ApJS*, 35, 441. doi:10.1086/190487
- Guo, Y., Zhang, B., Liu, C., et al. 2021b, arXiv:2110.06246
- Guo, Y., Li, J., Xiong, J., et al. 2021a, arXiv:2109.09775
- Hou, W., Luo, A., Yang, H., et al. 2015, *MNRAS*, 449, 1401. doi:10.1093/mnras/stv176
- Huang, W. & Gies, D. R. 2006a, *ApJ*, 648, 591. doi:10.1086/505783
- Huang, W. & Gies, D. R. 2006b, *ApJ*, 648, 580. doi:10.1086/505782
- Huang, W., Gies, D. R., & McSwain, M. V. 2010, *ApJ*, 722, 605. doi:10.1088/0004-637X/722/1/605
- Hunter, J. D. 2007, *Comput. Sci. Eng.*, 9, 90
- Kurucz, R. L. 2005, *Mem. Soc. Astron. It. Suppl.*, 8, 189
- Langer, N. 2012, *ARA&A*, 50, 107. doi:10.1146/annurev-astro-081811-125534
- Li, G., Van Reeth, T., Bedding, T. R., et al. 2019, *MNRAS*, 487, 782. doi:10.1093/mnras/stz1171
- Li, J., Liu, C., Zhang, B., et al. 2021, *ApJS*, 253, 45. doi:10.3847/1538-4365/abe1c1
- Li, X., Lu, Y., Comte, G., et al. 2015, *ApJS*, 218, 3. doi:10.1088/0067-0049/218/1/3
- Lindgren, L., Bastian, U., Biermann, M., et al. 2021, *A&A*, 649, A4. doi:10.1051/0004-6361/202039653
- Liu, C., Cui, W.-Y., Zhang, B., et al. 2015, *RAA*, 15, 1137. doi:10.1088/1674-4527/15/8/004
- Liu, C., Fu, J., Shi, J., et al. 2020, *RAA*, submitted; arXiv:2005.07210
- Liu, Z., Cui, W., Liu, C., et al. 2019, *ApJS*, 241, 32. doi:10.3847/1538-4365/ab0a0d
- Luo, A.-L., Zhao, Y.-H., Zhao, G., et al. 2015, *RAA*, 15, 1095. doi:10.1088/1674-4527/15/8/002
- Majewski, S. R., Schiavon, R. P., Frinchaboy, P. M., et al. 2017, *AJ*, 154, 94. doi:10.3847/1538-3881/aa784d
- Meynet, G. & Maeder, A. 1997, *A&A*, 321, 465
- Meynet, G. & Maeder, A. 2000, *A&A*, 361, 101
- Morgan, W. W., Sharpless, S., & Osterbrock, D. 1952, *AJ*, 57, 3. doi:10.1086/106673
- Ness, M., Hogg, D. W., Rix, H.-W., et al. 2015, *ApJ*, 808, 16. doi:10.1088/0004-637X/808/1/16
- O'Donnell, J. E. 1994, *ApJ*, 422, 158. doi:10.1086/173713
- Palacios, A., Gebran, M., Josselin, E., et al. 2010, *A&A*, 516, A13. doi:10.1051/0004-6361/200913932
- Poelarends, A. J. T., Herwig, F., Langer, N., et al. 2008, *ApJ*, 675, 614. doi:10.1086/520872
- Preston, G. W. 1974, *ARA&A*, 12, 257. doi:10.1146/annurev-aa.12.090174.001353
- Przybilla, N., Nieva, M.-F., & Butler, K. 2011, *Journal of Physics Conference Series*, 328, 012015. doi:10.1088/1742-6596/328/1/012015
- Ren, F., Chen, X., Zhang, H., et al. 2021, *ApJL*, 911, L20. doi:10.3847/2041-8213/abf359
- Riello, M., De Angeli, F., Evans, D. W., et al. 2021, *A&A*, 649, A3. doi:10.1051/0004-6361/202039587
- Rivinius, T., Carciofi, A. C., & Martayan, C. 2013, *A&A Rv*, 21, 69. doi:10.1007/s00159-013-0069-0
- Royer, F., Gerbaldi, M., Faraggiana, R., et al. 2002a, *A&A*, 381, 105. doi:10.1051/0004-6361:20011422
- Royer, F., Grenier, S., Baylac, M.-O., et al. 2002b, *A&A*, 393, 897. doi:10.1051/0004-6361:20020943
- Schlafly, E. F. & Finkbeiner, D. P. 2011, *ApJ*, 737, 103. doi:10.1088/0004-637X/737/2/103
- Skrutskie, M. F., Cutri, R. M., Stiening, R., et al. 2006, *AJ*, 131, 1163. doi:10.1086/498708
- Soubiran, C., Le Campion, J.-F., Brouillet, N., et al. 2016, *A&A*, 591, A118. doi:10.1051/0004-6361/201628497
- Sun, W., Li, C., Deng, L., et al. 2019, *ApJ*, 883, 182. doi:10.3847/1538-4357/ab3cd0
- Taylor, M. B. 2005, *ADASS XIV*, 347, 29
- Ting, Y.-S., Conroy, C., Rix, H.-W., et al. 2017a, *ApJ*, 843, 32. doi:10.3847/1538-4357/aa7688
- Ting, Y.-S., Conroy, C., Rix, H.-W., et al. 2019, *ApJ*, 879, 69. doi:10.3847/1538-4357/ab2331
- Ting, Y.-S., Rix, H.-W., Conroy, C., et al. 2017b, *ApJL*, 849, L9. doi:10.3847/2041-8213/aa921c
- Townsend, R. H. D., Owocki, S. P., & Howarth, I. D. 2004, *MNRAS*, 350, 189. doi:10.1111/j.1365-2966.2004.07627.x
- Venn, K. A. 1995, *ApJS*, 99, 659. doi:10.1086/192201
- Wade, R. A. & Rucinski, S. M. 1985, *A&AS*, 60, 471
- Wang, R., Luo, A.-L., Chen, J.-J., et al. 2020, *ApJ*, 891, 23. doi:10.3847/1538-4357/ab6dea
- Worthey, G., Faber, S. M., Gonzalez, J. J., et al. 1994, *ApJS*, 94, 687. doi:10.1086/192087
- Wu, X., Li, C., de Grijs, R., et al. 2016, *ApJL*, 826, L14. doi:10.3847/2041-8205/826/1/L14
- Xiang, M., Ting, Y.-S., Rix, H.-W., et al. 2019, *ApJS*, 245, 34. doi:10.3847/1538-4365/ab5364
- Xu, Y., Bian, S. B., Reid, M. J., et al. 2018, *A&A*, 616, L15. doi:10.1051/0004-6361/201833407
- Zhang, B., Liu, C., & Deng, L.-C. 2020a, *ApJS*, 246, 9. doi:10.3847/1538-4365/ab55ef
- Zhang, B., Liu, C., Li, C.-Q., et al. 2020b, *RAA*, 20, 051. doi:10.1088/1674-4527/20/4/51

Zhang, B., Li, J., Yang, F., et al. 2021, ApJS, in press;  
arXiv:2105.11624

Zhao, G., Zhao, Y.-H., Chu, Y.-Q., et al. 2012, RAA, 12,  
723. doi:10.1088/1674-4527/12/7/002

Zhongrui, B. 2013, The Intriguing Life of Massive Galaxies,  
295, 189. doi:10.1017/S1743921313004766

Zorec, J.&Royer,F. 2012,A&A, 537, A120.

doi:10.1051/0004-6361/201117691